AD-A253 993

RL-TR-92-23
Final Technical Report
February 1992

BEAM-PLASMA INTERACTIONS AND RADIATION GENERATION DURING THE EJECTION OF ELECTRON AND ION BEAMS IN SPACE

Institute of Geophysics and Planetary Physics (IGPP)

M. Ashour-Abdalla, H. Okuda, P.L. Pritchett, D. Schriver

DTIC
SELECTE
AUG 1 1 1992
S   B   D

92-22330

92   8   7 052

This report has been reviewed by the Rome Laboratory Public Affairs Office (PA) and is releasable to the National Technical Information Service (NTIS). At NTIS it will be releasable to the general public, including foreign nations.

RL-TR-92-23 has been reviewed and is approved for publication.

APPROVED:

JAMES ERNSTMEYER
Project Engineer

FOR THE COMMANDER:

JOHN K. SCHINDLER
Director
Electromagnetics & Reliability Directorate

REPORT DOCUMENTATION PAGE

1. AGENCY USE ONLY (Leave Blank)	2. REPORT DATE	3. REPORT TYPE AND DATES COVERED
	February 1992	Final Mar 88 - Nov 91

4. TITLE AND SUBTITLE

BEAM-PLASMA INTERACTIONS AND RADIATION GENERATION DURING THE EJECTION OF ELECTRON AND ION BEAMS IN SPACE

6. AUTHOR(S)

M. Ashour-Abdalla, H. Okuda, P.L. Pritchett, D. Schriver

5. FUNDING NUMBERS

C - F19628-88-K-0022
PE - 61102F
PR - 2305
TA - J2
WU - 57

7. PERFORMING ORGANIZATION NAME(S) AND ADDRESS(ES)
Institute of Geophysics and Planetary Physics (IGPP)
405 Hilgard Avenue
Los Angeles CA 90024-1567

8. PERFORMING ORGANIZATION REPORT NUMBER

N/A

9. SPONSORING/MONITORING AGENCY NAME(S) AND ADDRESS(ES)

Rome Laboratory (ERCP)
Hanscom AFB MA 01731-5000

10. SPONSORING/MONITORING AGENCY REPORT NUMBER

RL-TR-92-23

11. SUPPLEMENTARY NOTES
Rome Laboratory Project Engineer: James Ernstmeyer/ERCP/(617) 377-8977

12a. DISTRIBUTION/AVAILABILITY STATEMENT

Approved for public release; distribution unlimited.

12b. DISTRIBUTION CODE

13. ABSTRACT (Maximum 200 words)
Multi-dimensional electrostatic and electromagnetic particle simulations are used to investigate the nature of beam-plasma interactions and radiation generation during the injection of dense electron beams into the ionosphere from spacecraft. The nature of the injection process is determined primarily by the relative value of two characteristic time scales: the beam stagnation time t_s and the plasma response time t_{rp}. When $t_s < t_{rp}$, spacecraft charging is significant and most of the beam electrons are drawn back into the spacecraft. When $t_s > t_{rp}$, vehicle charging is reduced and the beam propagates away from the source. In this latter case there is strong beam-plasma turbulence which destroys the coherence of the beam within one or two gyroperiods. The spatial distribution of the beam has the form of a hollow cylinder near the source. As the beam propagates away from the source, the cylinder becomes increasingly filled. Return currents are associated with the field-aligned flow of ambient electrons, while current closure is provided primarily by the cross-field motion of the ions. The beam-plasma interaction leads to the formation of coherent current structures. Whistler waves with a peak in the frequency range $0.5 - 0.7 \Omega_e$ are produced by these structures via a coherent Cerenkov interaction. The Whistler waves propagate at angles substantially away from the resonance cone are are predominantly electromagnetic in nature.   (Cont'd)

14. SUBJECT TERMS Active experiments, Electron Beams, Cerenkov resonance, Whistler waves, Coherent radiation, Particle simulation Beam-plasma interaction, Spacecraft charging

15. NUMBER OF PAGES
68

16. PRICE CODE

17. SECURITY CLASSIFICATION OF REPORT	18. SECURITY CLASSIFICATION OF THIS PAGE	19. SECURITY CLASSIFICATION OF ABSTRACT	20. LIMITATION OF ABSTRACT
UNCLASSIFIED	UNCLASSIFIED	UNCLASSIFIED	UL

Block 13 (Cont'd)

To accurately measure cold plasma in the Earth's magnetosphere, the surface
potential of the spacecraft needs to be actively controlled to be near that of
the ambient plasma potential. To achieve this goal for the upcoming Geotail
and Cluster satellite missions, an ion emitter instrument that injects indium
ions from the spacecraft will be used. To understand the beam-plasma interaction
that can occur due to the ejection of the ion beam into the various regions
of the Earth's magnetosphere, a linear theory study has been carried out to see
whether particular combinations of ambient plasma parameters and ion beam
emission modes exist such that plasma instabilities may be excited.

Accession For

NTIS GRA&I
DTIC TAB
Unannounced
Justification

By
Distribution/
Availability Codes

Dist   Avail and/or
         Special

DTIC QUALITY INSPECTED 8

TABLE OF CONTENTS

PART A. ELECTRON BEAM EXPERIMENTS

Section

PART B.   SPACECRAFT POTENTIAL CONTROL VIA INDIUM
           ION BEAM INJECTION

Section

LIST OF FIGURES

iii

PART A. ELECTRON BEAM EXPERIMENTS

I. INTRODUCTION

Experiments involving the injection of electron beams into space plasmas have been carried out for over two decades. The motivations behind these experiments have been varied, ranging from investigations of charge neutralization processes in the plasma medium near the beam source to probing conditions on remote sections of geomagnetic field lines (see the reviews by *Winckler* [1980], in the monograph edited by *Grandal* [1982], and by *Maehlum* [1988]). The success of these injection experiments has led in recent years to the emergence of "active" or "controlled" experiments as a major technique in space physics research, both as a means for investigating the structure of the ionosphere and magnetosphere and for conducting studies in basic plasma physics.

A central physics question in active electron beam experiments is the nature of the interaction between the beam and the ambient plasma. The use of particle simulations to investigate the nonlinear plasma physics involved in such beam-plasma interactions dates back to roughly the same period [*Dawson and Shanny*, 1968] as the first beam experiments in space. Most of the previous two-dimensional simulations, however, have assumed periodic boundary conditions in one or both of the spatial coordinates. This assumption is certainly not appropriate for modeling injection experiments in space. In this report we employ a two-dimensional, isolated-system simulation model [*Pritchett and Winglee*, 1987; *Winglee and Pritchett*, 1988] to study aspects of beam-plasma interaction and radiation generation during active experiments. In this simulation model the spacecraft, beam, and ambient plasma are treated as an isolated system. The model provides a self-consistent treatment of the charging of the spacecraft together with the beam dynamics, electric and magnetic field formation, and plasma response both parallel and perpendicular to the magnetic field. It has the great advantage of providing a global perspective from which one can sort out the competing physical processes associated with the injection of the electron beam. Because the environment in the vicinity of a spacecraft is far from being spatially homogeneous, this is often difficult to do in space, especially when instruments are limited to one or two space vehicles.

II. SIMULATION MODEL

Our simulations of the beam-injection experiments employ the Beams-In-Geospace (BIG) code, which is a two-dimensional (but with all three velocity components) electrostatic particle simulation code for an isolated system. The BIG code has been described previously by *Pritchett and Winglee* [1987]. Here we briefly review the essential features. The spacecraft, beam, and ambient plasma are treated as an isolated system. The solution of Poisson's equation is obtained by convolving the Fourier transform of the charge density on the spatial grid with that of the Green's function for a single particle. The surface of the spacecraft is treated as an equipotential, which is accomplished through the use of the capacitance matrix [*Hockney*, 1968].

The configuration employed in the simulations is illustrated in Figure 1. The ambient magnetic field is assumed to be uniform and points in the x direction. The spacecraft has an idealized rectangular shape and is immersed in a uniform ambient plasma. The spacecraft is located well away from any boundaries, so that it can draw return currents from both the front and back sides. The beam electrons are injected from the right-hand side of the spacecraft. The injection velocity is taken to be monoenergetic, and the injection angle relative to the magnetic field can be varied between 0° and 90°. The velocity component along the magnetic field is denoted by v_{xb} and the component perpendicular to the field by v_{yb}. For each electron injected into the plasma, the spacecraft is given an opposite charge. If a plasma particle or a returning beam electron strikes the spacecraft, it is removed from the system and its charge is added to that on the spacecraft.

It is not possible to model precisely the various length scales and density ratios present in the injection experiments. Thus, the beam typically has a width of a few centimeters, while the spacecraft from which it is injected has a length of several up to tens of meters. The beam density at injection is of the order of 10^7 cm^{-3}, while the ambient plasma density is only of the order of 10^5 cm^{-3}. We choose the spacecraft size to be of the order of that for the rocket experiments, and we normally take the beam width to be the minimum allowable in the simulations, i.e., 2Δ, where Δ is the grid spacing. The beam density n_{bo} at injection is taken to be such that the total
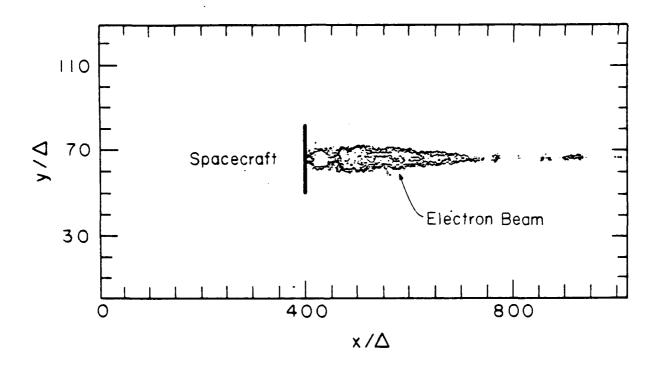
Figure 1. Configuration used in the isolated-system simulation model for beam injection. The rectangular spacecraft is located on a two-dimensional grid well away from all boundaries. It is immersed in a uniform ambient plasma, and the uniform magnetic field points in the x direction. The beam electrons are emitted from the right-hand edge of the spacecraft. For a typical rocket experiment the grid spacing Δ corresponds to about 10 cm.

current integrated over the assumed beam width is comparable to that in the actual experiment. This is not a limiting assumption since the actual beam tends to expand to a width of the order of the beam Debye length $\lambda_{Db} \equiv v_{xb}/\omega_{pb} \sim 5\Delta$ due to the electrostatic repulsive forces within the beam. Here, $\omega_{pb} = (4\pi n_{bo}e^2/m_e)^{1/2}$ is the beam plasma frequency at injection. For the case of the 1-keV electron gun used on the CHARGE rocket flights [*Raitt et al.*, 1984; *Myers et al.*, 1986; *Sasaki et al.*, 1986] and on the Space Shuttle flight STS-3 [*Inan et al.*, 1984; *Shawhan et al.*, 1984], Δ corresponds to about 10 cm and n_{bo} is of the order of $4 \times 10^5\,cm^{-3}$.

The dimensions of the simulation box are typically $L_x \times L_y = 1024\Delta \times 128\Delta$, so that the actual system size is about 100 m $\times$ 13 m. While one would like to treat a larger system, this is sufficient to accommodate many of the important processes occurring in the near environment of the injection point. The spacecraft normally has dimensions of $4\Delta \times 32\Delta$ and is usually located with its left-hand side at $x/\Delta = 400$.

The electrons and ions comprising the ambient plasma are represented by superparticles. For the plasma electrons, the charge-to-mass ratio is the same as for the beam electrons, and the charge is adjusted so that the initial density of the plasma relative to the injected beam density has the desired value n_{eo}/n_{bo}. The mass of the plasma ions is taken to be 100 times the mass of the plasma electrons. Typically, 160,000 superparticles are used to represent each plasma species. The initial velocity distributions of the plasma electrons and ions are Maxwellians with $T_e = T_i$ and a thermal velocity $v_{Te} = 0.5\,\Delta\omega_{pb} = 0.1\,v_{xb}$.

The basic isolated-system model has been extended to include the self-consistent solution of the full set of Maxwell's equations [*Winglee and Kellogg*, 1990; *Pritchett*, 1991]. The electromagnetic (or transverse) fields $\underset{\sim}{E}_T$ and $\underset{\sim}{B}$ are determined from the transverse current density $\underset{\sim}{J}_T$ using a standard leapfrog algorithm [*Pritchett*, 1985]. The particles are then pushed using the full relativistic Lorentz force equation. This extended model will be used in the investigation of whistler wave generation from electron beams.

III. CHARACTERISTIC INJECTION TIME SCALES

There are two characteristic time scales which determine the ability of the beam to escape from the near environment of its source [*Winglee and Pritchett*, 1987; *Pritchett and Winglee*, 1987]. The first is the beam stagnation time t_s. This is defined to be the time required for the first beam electron to be brought to rest under the influence of the positively-charged spacecraft for injection into vacuum. The corresponding distance away from the injection point where the first electron comes to rest is called the stagnation distance x_s. In one dimension (the case of an infinitely wide beam) $t_s = 2 \omega_{pb}^{-1}$ independent of the beam velocity, and $x_s = 0.5 \lambda_{Db}$. Here $\lambda_{Db} = v_b/\omega_{pb}$ is the beam Debye length.

In order to determine the properties of t_s and x_s in two dimensions, we performed a series of simulations for parallel injection into vacuum for different beam widths and energies. The results are given in Tables 1 and 2. In these results the spacecraft length is kept fixed at 32Δ.

TABLE 1.   Stagnation Time t_s and Stagnation Distance x_s as
a Function of Beam Width w_b

w_b/Δ	$\omega_{pb}t_s$	x_s/λ_{Db}
2	8.9	1.3
4	5.4	1.1
8	3.4	0.8
16	2.5	0.6
32	2.2	0.5

Table 1 illustrates the dependence on the beam width with the injection velocity fixed at $v_b = 5 \Delta\omega_{pb}$. As the beam width is increased above $\lambda_{Db} = 5\Delta$ toward the spacecraft size, t_s and x_s decrease toward their one-dimensional limits. This case is not relevant to the active experiments, however, since normally the initial beam width (of order a few cm) is smaller than λ_{Db} (~10 cm). At the smallest value of $w_b = 2\Delta$, t_s is larger by a factor of more than 4 compared to the one-dimensional limit. This increase in t_s with

decreasing beam width is due to (i) the amount of current (and hence charge) emitted decreases with w_b (assuming n_b is fixed) so that the rate of charging of the spacecraft is reduced and (ii) the distance from the beam over which the spacecraft charge is distributed increases so that the effective force on the beam electrons decreases.

TABLE 2.   Stagnation Time t_s and Stagnation Distance x_s as
a Function of Beam Debye Length λ_{Db}

λ_{Db}/Δ	$\omega_{pb}t_s$	x_s/λ_{Db}
2.5	6.0	1.2
5.0	8.9	1.3
10.0	12.5	1.7
20.0	18.6	2.3

Table 2 shows the dependence of t_s and x_s on the beam speed for a fixed width of $w_b = 2\Delta$. Both t_s and x_s increase with increasing v_b. This occurs despite the accompanying increase in the charging rate because the charging increases only at a rate proportional to v_b, while the potential required to bring the beam electrons to rest increases at a rate proportional to the beam energy, i.e., to v_b^2. The actual values of t_s are seen to be approximately proportional to $v_b^{1/2}$.

The second characteristic time scale associated with the beam injection is the plasma response time t_{rp}. This is the time required for the ambient plasma to respond to the fields produced by the injection of the electron beam. t_{rp} is determined by the ambient density, $t_{rp} \approx \sqrt{3}/\omega_{pe}$, where ω_{pe} is the ambient plasma frequency. The relative value of t_s and t_{rp} determines two characteristic injection regimes. When t_s is the shorter time, there is not sufficient time for return currents to flow and neutralize the spacecraft before the stagnation region forms. In this case there will be strong vehicle charging and low injection efficiency. If, on the other hand, t_{rp} is the shorter time, then the spacecraft will be neutralized before the stagnation region has a chance to form. In this case the injection efficiency will be high.

IV. SPACECRAFT CHARGING

Figure 2 shows the time histories of the spacecraft charge Q_c (normalized to the amount of charge injected in a time $t = 1/\omega_{pb}$) and the spacecraft potential Φ (normalized to the beam potential) for the case of injection parallel to the magnetic field with no ambient plasma present. The charge and potential on the spacecraft increase very rapidly on a time scale of the stagnation time ($\omega_{pb}t_s = 8.9$) until the potential reaches nearly the beam voltage. At this point the electric field is strong enough to begin returning beam electrons to the spacecraft. A quasi-steady state is then established during which the number of returning electrons balances the number of newly injected electrons, and thus the spacecraft charge remains constant. During this time it is apparent that the spacecraft potential increases slowly and reaches a value 40% above the beam voltage by the end of the run. This occurs because of the continued propagation away from the spacecraft of the initial electrons injected before the stagnation region forms. As they recede, their contribution to the electric field at the spacecraft decreases, and the floating potential of the spacecraft increases. The potential drop across the stagnation region remains equal to the beam voltage, however. During the early stage when the charge and potential on the spacecraft increase in unison, we can determine a capacitance for the spacecraft. From the curves in Figure 2 we find that the capacitance per unit length is about 8×10^{-11} F/m.

When there is an ambient plasma present, the spacecraft will initially begin charging rapidly since it takes a finite time ($\sim 1/\omega_{pe}$) for the return currents to begin flowing. If the stagnation time $t_s \lesssim$ the plasma response time t_{rp}, then the spacecraft potential will reach nearly the full beam energy. At later times there is an appreciable return current to the spacecraft carried by the ambient electrons. For $n_{eo}/n_{bo} = 1/32$, for example, the number of beam electrons remaining in the system increases at a rate that is about 20% of the injection rate. This ambient return current and the neutralization of the beam front by the ambient plasma combine to keep the potential roughly constant in time at about 70% of the beam voltage. If the ambient plasma density is increased so that $t_{rp} < t_s$, then the period of rapid charging is of greatly reduced duration. For example, with $n_{eo}/n_{bo} = 1/4$ (which gives $\omega_{pb}t_{rp} = 3.4$), the ambient plasma is able to provide almost the
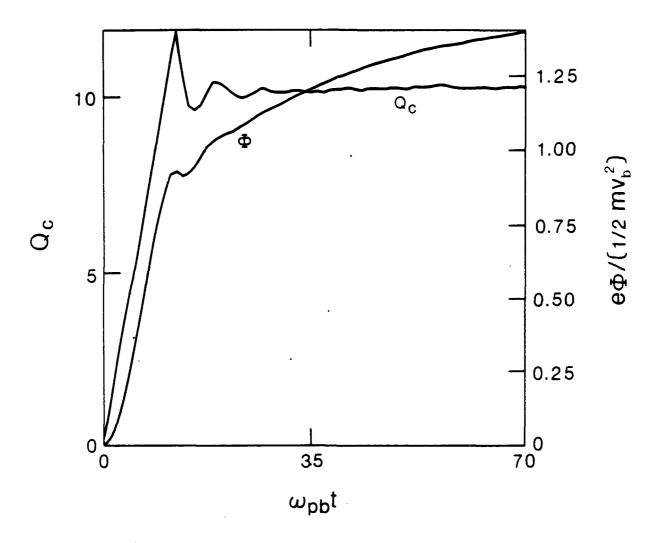
Figure 2. <u>Time histories of the spacecraft charge Q_c (normalized to the charge injected in time $t = 1/\omega_{pb}$) and the spacecraft potential energy $e\Phi$ (normalized to the beam energy $mv_b^2/2$) for parallel injection into vacuum.</u>

entire return current, and the number of beam electrons in the system increases at about 85% of the injection rate. The potential then fluctuates near 20% of the beam voltage.

V. OBLIQUE INJECTION: BEAM PROPERTIES

As we have seen in the previous sections, when the plasma response time is shorter than the beam stagnation time, then the ambient plasma has sufficient time to respond to the beam injection and produce charge-neutralization of the spacecraft. The bulk of the beam electrons are then able to escape from the immediate vicinity of the spacecraft. However, as we shall now see, the beam is subject to strong distortion or disruption as it propagates away from the spacecraft. We shall consider a standard case where the beam is injected at 45° to the magnetic field into a plasma with density $n_{eo} = 0.25\ n_{bo}$. The parameters are $w_b = 2\Delta$, spacecraft length $L_{cy} = 32\Delta$, $v_{xb} = v_{yb} = 10\ v_{Te} = 5\ \Delta\omega_{pb}$, and $\Omega_e/\omega_{pb} = 0.5$.

In order to understand the mechanism which can lead to beam distortion for cross-field injection, Figure 3 shows the $v_x - x$ and $v_y - x$ phase spaces for the beam electrons at four different times during the simulation. It is seen from the parallel velocities (Figures 3a, c, e, and g) that at the earliest time a stagnation region develops with some of the beam electrons being drawn back into the spacecraft with v_x approximately equal to $-v_{xb}$. However, at later times when the plasma has had time to respond to the beam injection, the stagnation region is seen to expand outwards. This expansion is marked by a front (hereafter called the stagnation front, as opposed to the actual beam front) where the beam electrons experience strong deceleration with the velocity of some of the beam electrons changing sign. This stagnation front propagates outwards much more slowly than the beam front with an average speed of about $v_{xb}/3$ during the length of the simulation. Those electrons which are not confined behind the stagnation front are seen to excite space-charge oscillations as evidenced by the vortices ahead of the front in Figures 3e and g.

The effect of the formation of the stagnation front and the induced space-charge oscillations on the gyromotion of the electrons can be seen from the $v_y - x$ phase spaces shown in Figures 3b, d, f and h. The single-particle trajectory for an electron (neglecting wave-particle interactions) would be a helix, which, when projected onto the $v_y - x$ phase space, would appear as a sinusoidal curve. Such a sinusoidal curve (hereafter called the primary helix) can be seen in Figure 3b for those electrons propagating outwards and which have not yet reached the stagnation front. Those
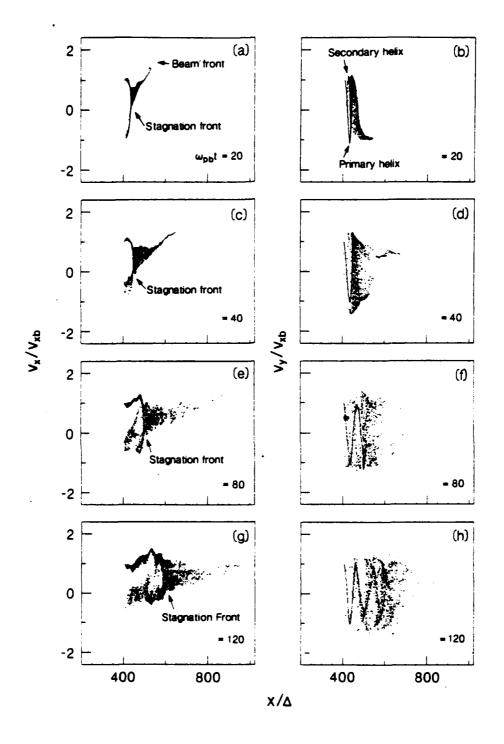
Figure 3. The $v_x - x$ phase space (left-hand side) and the $v_y - x$ phase space (right-hand side) for the beam electrons at times $\omega_{pb}t$ equal to 20, 40, 80, 120 for the case of injection at 45° to the magnetic field with the density ratio $n_{eo}/n_{bo} = 1/4$ and magnetic field strength $\Omega_e/\omega_{pb} = 0.5$.

electrons which are reflected at the stagnation front produce secondary helices which are backward propagating (e.g. Figures 3b and d). Ahead of the stagnation front, the large parallel velocity spread produced by the space-charge oscillations destroys any coherent helical motion except possibly near the beam front. At the latest time (Figure 3), a well-defined primary helix can be seen only over about 1.5 gyrations between $400 < x/\Delta \lesssim 550$ even though the beam front is well beyond this point. Thus, both the spacecraft charging and induced space-charge oscillations tend to randomize the parallel beam motion so that a well-defined helical motion (which is expected from single-particle trajectories) is no longer present.

The modification of the particle trajectories can also be seen in the contours of the beam density shown in Figure 4 for the same times as in Figure 3. Consecutive contours differ by a factor of $\sqrt{2}$. The primary helix is seen to advance outwards to about 550Δ after which it becomes incoherent. The formation of a secondary helix can be seen in Figures 4a and b. As the beam continues to break up, the region out to a beam gyroradius becomes filled with beam electrons as their trajectories are modified by the spacecraft charging and the induced space-charge oscillations. In three dimensions these electrons would actually lie on a hollow cylinder rather than a filled cylinder. This can be seen in Figure 5, which shows the $v_y - y$ phase space at $\omega_{pb}t = 120$ for beam electrons over (a) all x, (b) x between 400Δ and 550Δ (i.e., between the spacecraft and stagnation front) and (c) x between 550Δ and 700Δ (i.e., forward of the stagnation front). The trajectory of a gyrating electron (neglecting wave-particle interactions) in this phase space is a simple circle, and its trajectory in real space is a helix. In the present case, we have an ensemble of electrons which have approximately circular orbits in phase space. The corresponding real space trajectories (i.e., the ensemble of helices) lie on a hollow cylinder. This hollow cylinder has a radius approximately equal to a beam gyroradius and width of about 10Δ, which is equal to two beam Debye lengths. This thickness is much larger than the initial beam width due to repulsive forces associated with a net negative charge within the beam which cause it to expand radially. This cylinder is seen, on comparing Figures 5b and c, to become more filled in beyond the stagnation point due to the loss of perpendicular energy through the space-charge oscillations excited by the escaping beam electrons.
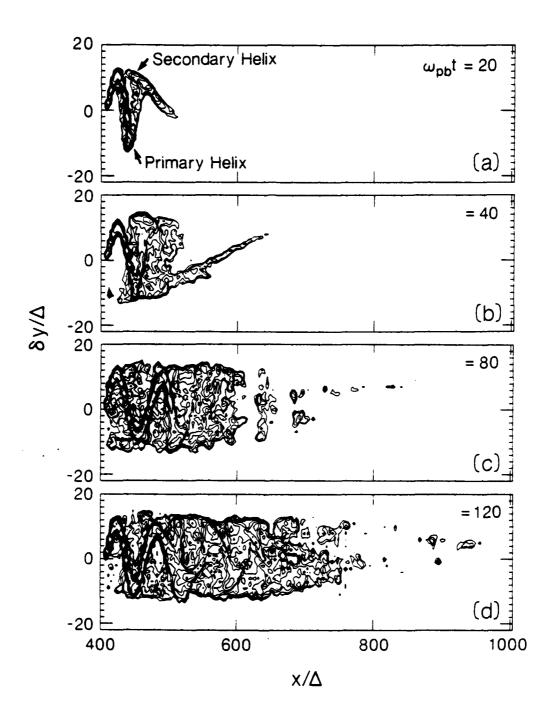
Figure 4. Contours of the beam density corresponding to the cases shown in Figure 3. Consecutive contours differ by a factor of $\sqrt{2}$. A coherent primary helix can be seen for only about one gyration from the point of injection.
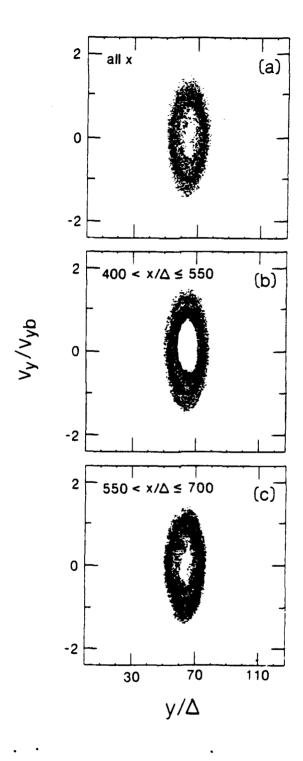
Figure 5. The $v_y - y$ phase space at $\omega_{pb}t = 120$ for the beam electrons computed over (a) all x, (b) x between 400 Δ and 550 Δ, and (c) x between 550 Δ and 700 Δ.

VI. OBLIQUE INJECTION: PLASMA RESPONSE

In order to illustrate the plasma response to the beam injection, Figure 6 shows contours of (a) the charge density of the beam and spacecraft, (b) the plasma electron density and (c) the plasma ion density at the end of the run at $\omega_{pb}t = 120$. The successive contours in Figure 6a differ by a factor of $\sqrt{10}$ so that both the primary helix and the dispersed low-density beam components can be seen. In Figures 6b and c, the contours decrease linearly from the maximum value down to 8% of the maximum value. The dotted areas denote regions where the density is smaller than the initial density. The arrows in Figure 6 show the plasma flows as determined from the particle phase space.

It is seen that forward of the stagnation front, there is an enhancement in the density of the plasma electrons on the same field lines as the beam electrons. This enhancement is produced by a push exerted by a repulsive force associated with the injection of the negative beam charge (the plasma electrons, being tied to the field lines, do not move significantly across the field lines). This acceleration produces the maximum in the plasma electron density of $0.46n_{bo}$ (= 1.8 n_{eo}) just forward of the secondary front at $x/\Delta \approx 550$.

Closer in towards the spacecraft there are depletions in the plasma electron density resulting from their motion towards the spacecraft, which forms a return current. Note, however, that the depletions extend beyond the length of the spacecraft. The field-aligned flow of electrons located above and below the spacecraft leads to the density enhancements seen behind the spacecraft.

Additional return currents are drawn from behind the spacecraft. This return current consists of the electrons on the field lines connected to and behind the spacecraft and results in the depleted plasma regions directly behind the spacecraft. The length of this depletion region increases at a speed comparable to that of the return current electrons that overshoot the spacecraft.

Current closure or charge-neutralization of the spatially separate beam and return currents is produced by the plasma ions being accelerated across the field lines [*Pritchett and Winglee*, 1987]. This is seen in Figure 6c, where the ions behind the spacecraft are accelerated outwards

15
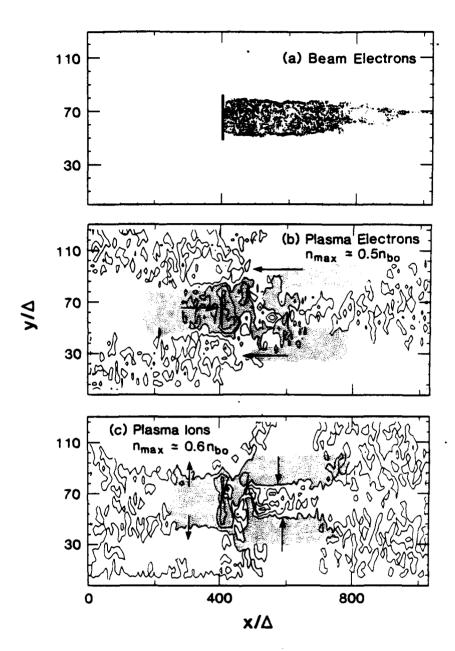
Figure 6. Contours of (a) the charge density of the beam and spacecraft, (b) the plasma electron density, and (c) the plasma ion density at $\omega_{pb}t = 120$ for the same conditions as in Figures 3–5. Successive contours in (a) differ by a factor of $\sqrt{10}$, while those in (b) and (c) decrease linearly from the maximum value down to 8% of the maximum value. The arrows in (b) and (c) indicate direction of the plasma flows in response to the beam injection. The shaded areas indicate regions where the density is smaller than the initial plasma density.

producing a local maximum of about 0.4 n_{bo} (= 1.6 n_{eo}) above and below the spacecraft. In front of the spacecraft, the ions are accelerated inwards towards the beam, producing a maximum plasma ion density of 0.6 n_{bo} (= 2.4 n_{eo}) in the center of the system. Note that as these ions are drawn inwards, they form a local maximum along the primary helix of the beam wherever it remains intact; forward of the stagnation front where the beam has lost its coherence, the ions do not accumulate along any helical structure.

VII. ELECTRON BEAM PROPAGATION IN THREE DIMENSIONS

One of the drawbacks of a two-dimensional model for beam experiments is that the collecting area on the source spacecraft can be no more than an order of magnitude larger than the beam area. In contrast, the actual ratio ranges from $\sim 10^3$ on sounding rockets to more than 10^4 on the shuttle. A three-dimensional model developed by *Okuda and Ashour-Abdalla* [1990a] allows one to model this large geometrical ratio. In this model the beam is injected from one face of the simulation box, with the entire face assumed to be a perfect conductor. Periodic boundary conditions are assumed in the direction transverse to the magnetic field. With a conductor surface area of $S = 64\Delta \times 64\Delta$ or $128\Delta \times 128\Delta$ [*Okuda and Ashour-Abdalla*, 1990b] and a beam cross-sectional area S_b of $4\Delta^2$, the ratio of S/S_b lies in the range of $1\sim4 \times 10^3$.

This three-dimensional model has been used to investigate the injection of a strongly overdense beam with $n_{bo} \gg n_{eo}$. The resulting presence of such a strong negative space charge causes the beam to expand radially outward already during the first plasma period. *The expansion continues until the beam density becomes approximately equal to the ambient density*, $n_b \approx n_{eo}$. The radial electric field causes an azimuthal $\underset{\sim}{E} \times \underset{\sim}{B}$ velocity pattern for both the beam and ambient electrons within the expanded beam region (Figures 7a and 7b). The maximum flow speeds for the beam and ambient electrons are 12.4 v_{Te} and 2.6 v_{Te}, respectively. The motion of the ions is quite different. On time scales less than the ion gyroperiod, they can respond directly to the radial electric field. As shown in Figure 7c at $\omega_{pe}t = 30$, the ions are accelerated inward across the magnetic field in order to neutralize the beam electrons.

Figure 8 shows the parallel phase space for the beam electrons at (a) $\omega_{pe}t = 20$ and (b) $\omega_{pe}t = 40$. In this case the injection density ratio is $n_{bo}/n_{eo} = 64$. It is apparent that even though there is strong modulation of the beam associated with the formation of trapping vortices, most of the beam electrons do propagate away from the conductor. In this simulation the ratio I_b/I_a of the beam current to the thermal return current is $I_b/I_a = 1.5$. Thus, due to the large conducting area, the ambient current is comparable to the beam current, and so the spacecraft potential remains small
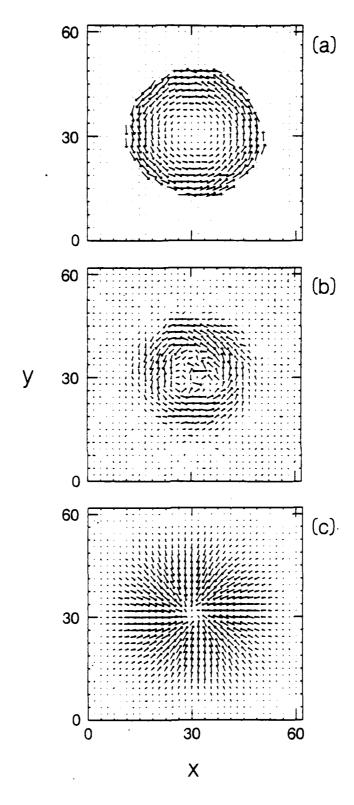
Figure 7. **Macroscopic flow velocity perpendicular to the magnetic field for the injection of an overdense beam in three dimensions: (a) beam electrons, (b) ambient electrons, and (c) ions at time $\omega_{pe}t = 30$.**
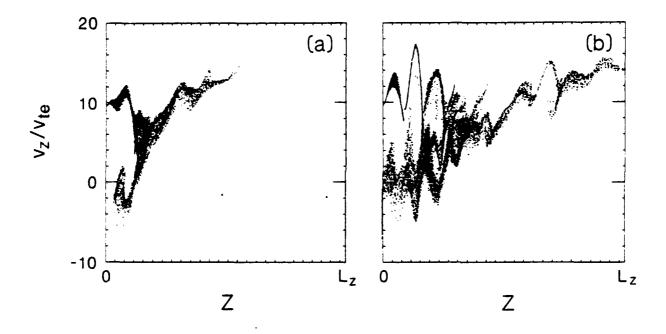
Figure 8.   Phase space plots of the beam electrons in (z,v_z) space at (a) $\omega_{pe}t = 20$ and (b) $\omega_{pe}t = 40$.   Here z denotes the coordinate parallel to the magnetic field.

compared to the beam energy. In this circumstance even a very overdense beam is able to escape from the injection region.

VIII. WHISTLER MODE RADIATION FROM ELECTRON BEAMS IN SPACE

The generation of whistler mode radiation has been observed in connection with a number of electron beam experiments in both plasma chambers [*Bernstein et al.*, 1979; *Kellogg and Monson*, 1981; *Kellogg et al.*, 1982] and in space [*Cartwright and Kellogg*, 1974; *Monson and Kellogg*, 1978; *Dechambre et al.*, 1980; *Beghin et al.*, 1984; *Gurnett et al.*, 1986; *Kellogg et al.*, 1986]. For example, during the Spacelab 2 mission the Plasma Diagnostics Package (PDP) performed a fly-around of the shuttle at distances of up to 300 m while an electron beam was being ejected from the shuttle. During a magnetic conjunction of the shuttle and the PDP, a funnel-shaped emission was detected below the electron cyclotron frequency Ω_e that was interpreted as being due to whistler emission from the electron beam [*Gurnett et al.*, 1986]. The generation mechanism of the whistler waves was not immediately evident. As noted by *Farrell et al.* [1988], the observed wave intensity, which was estimated to be about 3×10^{-5} of the beam power, was of the order of 10^7 times greater than expected on the basis of incoherent, single-particle radiation [*e.g., Mansfield*, 1967]. Thus some coherent radiation mechanism must have been involved. Since the beam width was less than one whistler wavelength, however, it is difficult to imagine that a conventional whistler instability could produce amplification within the narrow confines of the beam. *Farrell et al.* [1988] suggested that the mechanism could involve coherent Cerenkov radiation from electron bunching in space at the plasma frequency produced by an electrostatic beam-plasma instability.

In order to obtain some additional insight regarding the generation mechanism, we have carried out two-dimensional electromagnetic particle simulations of the beam-plasma interaction. The initial results, to be described in section IX, were obtained using a pure initial-value model. Subsequently, we have used the electromagnetic version of the isolated-system model. These results will be described in section X.

Figure 9 gives a schematic diagram of the initial-value simulation model. A dilute beam of field-aligned electrons is assumed to exist initially throughout the central region of the simulation box. In the results presented here, the beam density n_b is taken to be one quarter of the ambient
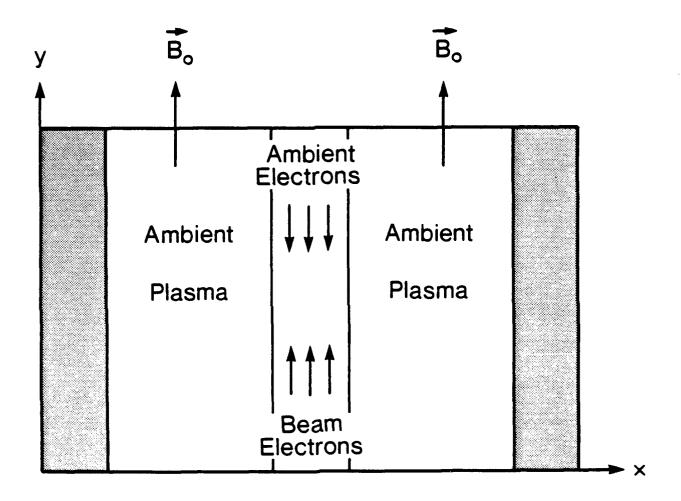
Figure 9. A schematic of the initial-value simulation model. The initial beam and return currents are field aligned and confined to the central portion (in x) of the simulation box.

density n_0, the beam energy is 5.7 keV, and the width of the beam is 14 m. The current carried by the electron beam must be balanced by a return current in the ambient plasma. To represent this current, we assign an initial drift of $-v_b/3$ to the ambient electrons located in the beam region (whose density is taken to be 3 $n_0/4$). Outside the beam region is a stationary ambient plasma of density n_0. The magnetic field is oriented in the y direction and has a strength such that $\Omega_e/\omega_{pe} = 0.3$. The simulation system is periodic in y but bounded in x. The ions are treated as a fixed neutralizing background.

IX. GENERATION MECHANISM OF WHISTLER MODE RADIATION

As is well known, the interaction of a weak beam with an ambient plasma leads to the excitation of electrostatic Langmuir oscillations with wavenumber k given by $k \approx \omega_{pe}/v_b$. In the present simulation this most unstable mode corresponds to mode 7 in the y direction. Figure 10a shows the time history of the parallel (y) component of the electrostatic energy for this mode. The exponential growth is already apparent by $\omega_{pe}t \sim 10$, and saturation occurs by $\omega_{pe}t \sim 25$. The linear growth rate is $0.23\ \omega_{pe}^{-1}$. The growth of the Langmuir oscillations leads to the well-known formation of vortices in the v_y–y phase space. The Langmuir oscillations are confined to the finite beam region, in agreement with Spacelab 2 observations [*Gurnett et al.*, 1986]. At saturation the total electrostatic field energy amounts to 14% of the initial beam energy. After saturation the Langmuir waves collapse as the beam-plasma system is thermalized.

Figures 10b and c show the time history of the z component of the magnetic field energy for the two longest wavelength modes in the system (modes 1 and 2 in the y direction). There is a clear exponential growth phase in both modes that becomes apparent above the background by $\omega_{pe}t \sim 20$. The rapid growth continues until $\omega_{pe}t \sim 30$; subsequently, the field energy remains at an enhanced level. In contrast, the magnetic field energies for modes 3–7 collapse back to the thermal level as the electrostatic waves decay. It is thus clear that persistent long-wavelength electromagnetic modes are being excited on a time scale comparable to that of the beam-plasma interaction.

To identify the nature of these electromagnetic modes, we examine the power spectra curves given in Figure 11. These spectra are measured well outside the beam region. The top two curves are for the y and z components of the magnetic field, while the bottom one is for the z component of the electric field. In all three cases the dashed curve represents the thermal level in the simulation in the absence of an electron beam, while the solid curve is the result with the electron beam. The magnetic plots show enhancements by factors of 80 and 20, respectively, above the thermal level in the frequency range below Ω_e. Otherwise, there is no significant wave excitation above the background level. The long-wavelength modes excited by the electron beam are thus clearly whistler waves.
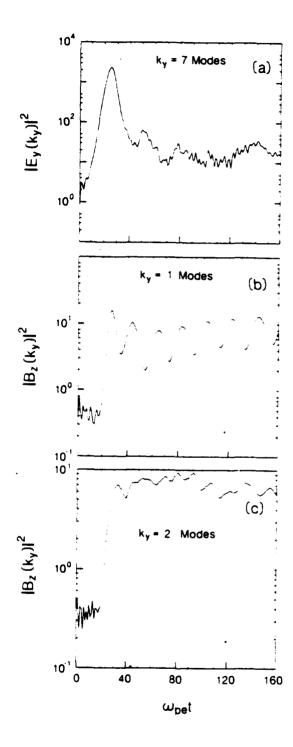
Figure 10. Time histories of (a) the y component of the electrostatic field energy for mode 7 and (b), (c) the z component of the magnetic field energy for modes 1 and 2.
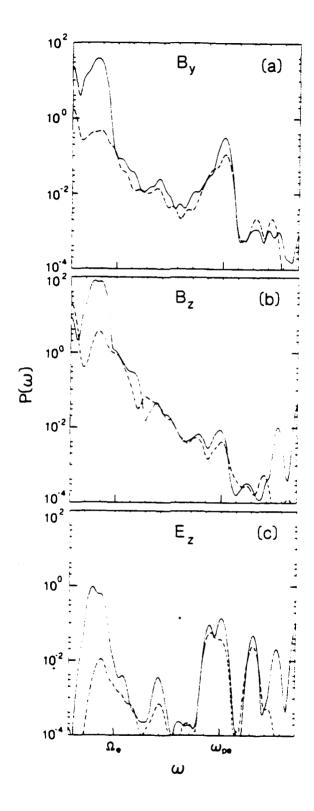
Figure 11. <u>Power spectra computed in the ambient plasma region at x = 80 and 176 averaged over all values of y for (a) B_y, (b) B_z, and (c) E_z.</u>

The wave vectors for the four most intense modes excited in the simulation make angles of 27°, 45°, 27° and 37° with respect to the magnetic field and have frequencies ω/Ω_e = 0.53, 0.50, 0.72, and 0.67, respectively. The corresponding resonance cone angles are 57°, 59°, 43°, and 47°. Thus the most intense whistler waves are propagating considerably away from the resonance cone. The total energy radiated as whistler waves is estimated to be 0.1% of the initial beam energy.

The present simulations show that the beam-plasma interaction produces a complex current structure with significant J_x, J_y, and J_z components. While the largest contribution is the mode 7 component associated with the dominant Langmuir wave, there are also substantial contributions in modes 1–6. The transverse components J_x and J_z arise from the existence of the electrostatic field in the x direction which accelerates the electrons perpendicular to the magnetic field and produces $\underset{\sim}{E} \times \underset{\sim}{B}$ drifts. Figure 12 shows time history plots of $|J_y(k_y)|^2$ and $|J_z(k_y)|^2$ for modes 1 (panel a) and 2 (panel b). The currents are computed from both the beam electrons and the ambient electrons in the original beam region. The dramatic growth in all four cases during the period from 15 ω_{pe}^{-1} to 30 ω_{pe}^{-1} illustrates the common origin of the current structure in the processes associated with the beam-plasma interaction. Although the current structure has significant components in modes 1 through 7, only the first two can satisfy the Cerenkov resonance condition $k_\parallel = \omega/v_\parallel$ with $\omega < \Omega_e$ and $v_\parallel \lesssim v_b$ and thus produce whistler waves. Since $|J_\parallel|^2 >> |J_\perp|^2$ in the simulations, one surmises that the whistler waves are generated predominantly by the $J_\parallel$ current. This conclusion is further strengthened by the single-particle analysis of *Mansfield* [1967] which shows that $v_\perp$ makes only a small contribution to the Cerenkov radiation level if $v_\perp \lesssim v_\parallel$.

The present initial-value simulations have demonstrated that whistler waves are produced from electron beams on the same time scale as the classical beam-plasma interaction whose dominant feature is the production of intense Langmuir oscillations. The growth of these electrostatic oscillations is accompanied by the formation of a current structure which acts like an antenna and emits whistler waves in a coherent manner. Since the generation efficiency in the simulations is so much higher than that actually observed, however, it is not yet clear that

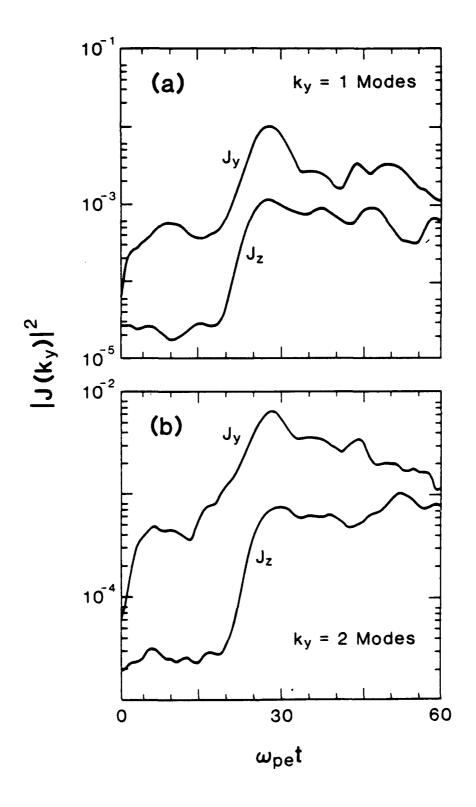Figure 12. <u>Time histories of $|J_y(k_y)|^2$ and $|J_z(k_y)|^2$ in the beam region for (a) mode 1 and (b) mode 2.</u>

this mechanism is actually the operative one in the beam experiments in space. We address this point in the next section.

X. WHISTLER MODE RADIATION FROM AN INJECTED ELECTRON BEAM

We now use the electromagnetic version of the BIG simulation code to reexamine the process of coherent whistler radiation from electron beams. This is a much more realistic model than the initial-value calculation since the beam is now injected at a single point. The configuration is similar to that shown in Figure 1; the beam energy is now higher (E_b = 16 keV), and the grid spacing Δ corresponds to about 40 cm. The magnetic field strength will be varied but is always such that the electron cyclotron frequency Ω_e is less than the ambient plasma frequency ω_{pe}, as was the case during the Spacelab 2 observations.

The most striking difference between the present continuous-injection simulations and the previous initial-value results is the sharply reduced level of electrostatic Langmuir oscillations. Instead of a rapid initial growth followed by collapse of these oscillations, there is now a slower build up of the parallel wave energy toward a quasi-static level on a time scale of 30–40 ω_{pb}^{-1}. The total electrostatic field energy is now only a few tenths of a percent of the energy of the beam *electrons injected during this interval*. The initial-value simulations thus appear to have overestimated significantly the strength of the beam-plasma interaction.

Figure 13 shows contours of the perturbed B_z field at times $\omega_{pb}t$ = 40, 80, and 120 for the case of Ω_e/ω_{pe} = 0.5. The current sheet formed by the injected electron beam produces an antisymmetric field relative to the beam axis. Superimposed on this dominant field are periodic modulations with a wavelength of ~ 90Δ. The direction of propagation relative to the ambient magnetic field appears to decrease as a function of time, from $\approx 10°$ at the earliest time to $\approx 4°$ at the latest time. The perturbed B_y field shows a similar wave pattern. Figure 14 shows power spectra measured at a point δx = 90 Δ, δy = 40 Δ relative to the beam injection point for the y and z components of the magnetic field and the y component of the transverse (electromagnetic) electric field. The B_y spectrum shows a clear peak at $\omega \approx$ 0.7 Ω_e; the E_y spectrum has a similar peak but with an intensity about two orders of magnitude weaker. We thus identify the wave disturbances as whistler waves propagating with a phase velocity of order c/10. The B_z spectrum shows a similar spectral intensity in the whistler region but it
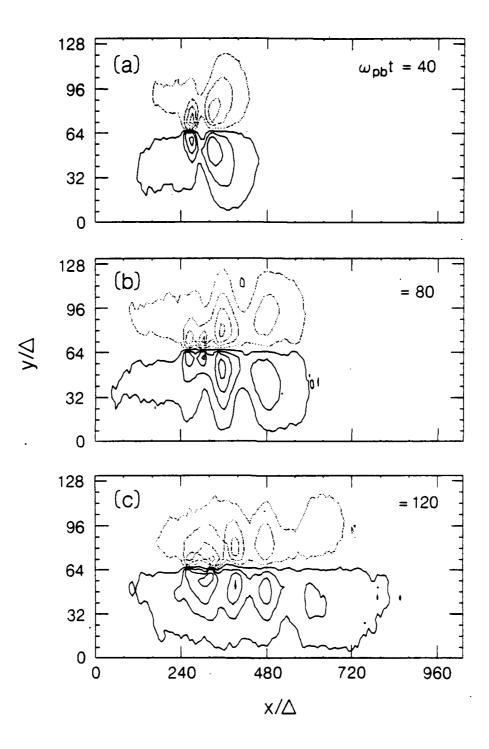
Figure 13. Contours of the B_z magnetic field resulting from the injection of an electron beam located at $x/\Delta = 245$ and $y/\Delta = 64$ into an ambient plasma with $\Omega_e/\omega_{pe} = 0.5$. Solid contours indicate positive values of B_z, while dotted contours indicate negative values.
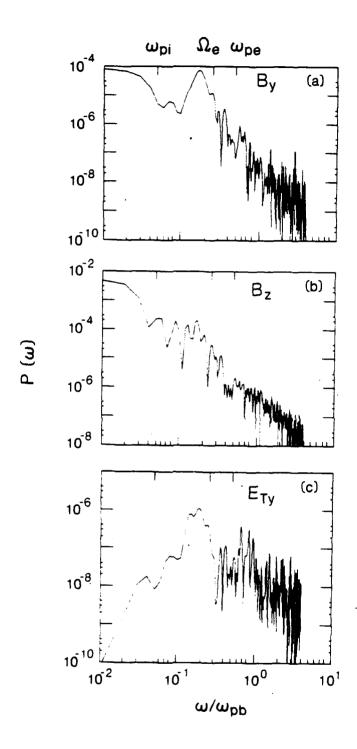
Figure 14. Power spectra for the B_y, B_z, and E_{Ty} fields averaged over the interval $0 < \omega_{pb}t < 200$ at a point $\delta x/\Delta = 90$, $\delta y/\Delta = 40$ away from the source of the electron beam. The ambient density is given by $\Omega_e/\omega_{pe} = 0.5$.

produces only a shoulder on the much larger fields associated with the current sheet. The intense peaks at frequencies $\lesssim \omega_{pi}$ are associated with the ion response to establish current closure across field lines.

Figure 15 shows the time history of the B_y and B_z fields at the same point $\delta x = 90\ \Delta$, $\delta y = 40\ \Delta$. During the interval up to $\omega_{pb}t \approx 100$, these fields are 90° out of phase and have peak-to-peak variations that are within 20% of each other. Thus the waves are nearly right circularly polarized. The total whistler wave energy is about 5×10^{-5} of the electron beam energy injected up to time $\omega_{pb}t = 80$. This is now consistent with the Spacelab 2 observations. Similar results are obtained for a second simulation with $\omega_{pe}/\Omega_{pe} = 0.3$ except that the angles of propagation are somewhat larger, ranging from ≈ 19° down to ≈ 8° as a function of time.

With the present simulation parameters the spacecraft potential increases slowly with time (after a rapid initial jump and decay) and reaches a level of $\approx 40\%$ of the beam energy by the end of the run ($\omega_{pb}t = 200$). As a result of this charging, the ambient electron density is reduced on field lines connected to the spacecraft. This leads to the formation of a density depression extending out from the spacecraft whose spatial extent along the magnetic field increases with time at a speed of $\approx v_b/3$. The average density decrease is about a factor of two, but there are local depressions of a factor of four or more. The establishment of this density trough has a significant effect on the propagation of the whistler waves. For $0.5 < \omega/\Omega_e < 1$, whistler waves can be trapped in a density trough which then acts as a duct [e.g. *Smith et al.*, 1960]. This explains the observed decrease in propagation angle of the waves as a function of time as the trough expands. The density depressions produced in the simulations are considerably larger than the values of 2–10% necessary for trapping. The termination of the whistler generation after $\omega_{pb}t \approx 80$ is presumably related to the modification of the beam-plasma interaction resulting from the formation of the density trough.

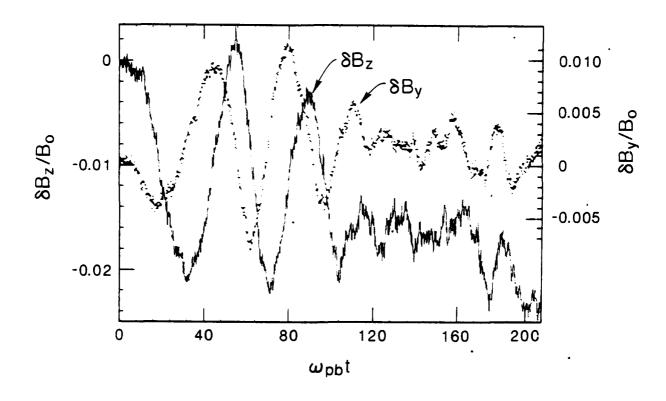Figure 15. Time history of the B_y and B_z fields at a point $\delta x/\Delta = 90$, $\delta y/\Delta = 40$ away from the source of the electron beam.

XI. SUMMARY

In recent years particle simulation models in two and three spatial dimensions have been developed to the extent that they can be used to investigate the physics of beam-plasma interactions in configurations that are representative of those present in active experiments in space. Such models have the possibility of providing a global perspective on the various processes involved in the beam-injection experiments and can thus serve as an important complement to the actual observations which are obtained on one or at most a few spacecraft.

We have used an isolated-system electrostatic model to study the beam properties and plasma response associated with the injection of an electron beam. We have seen that the nature of these processes is primarily determined by the ratio of the stagnation time t_s and the plasma response time $t_{rp} \simeq \sqrt{3} / \omega_{pe}$. When $t_{rp} > t_s$, then the beam dynamics is dominated by the formation of the stagnation region, and the beam electrons are confined in the immediate vicinity of the spacecraft. The spacecraft potential then rises to the order of the beam energy. When $t_{rp} < t_s$, however, the beam is able to escape from the near environment of the spacecraft. The primary factor in determining t_{rp}/t_s is the ratio of the ambient plasma density to the beam density [*Pritchett and Winglee*, 1987]. For a fixed value of this density ratio, the stagnation time is increased by decreasing the beam width and/or increasing the beam energy. Decreasing the width decreases the current emitted by the spacecraft and hence decreases the charging rate. It is then easier for the beam to propagate away from the injection region. While raising the beam energy leads to an increase in the charging rate which is proportional to the beam velocity, the spacecraft potential necessary to bring the beam to rest increases approximately with the beam energy (i.e., with the square of the beam velocity). As a result, the stagnation time actually increases at a rate proportional to the square root of the parallel beam velocity. Thus, a thin beam of high energy is able to propagate away from the spacecraft more easily than a thick low energy beam.

Even in the cases where there is no strong charging and the beam can escape from the near environment of the spacecraft, the beam is subject to strong distortion due to the electric fields arising from the space-charge oscillations produced by the beam-plasma interaction. For cross-field

injection these fields tend to randomize the beam electrons and thus destroy the coherent nature of the beam associated with its gyromotion. The helical structure in the beam persists for only one or two gyrations. After that, the beam electrons are scattered onto a hollow cylinder with a width of about two beam Debye lengths.

The plasma response to the beam injection forward of the spacecraft consists of a field-aligned flow of electrons along field lines adjacent to the beam towards the spacecraft coupled with perpendicular acceleration of the ions on these field lines into the beam to provide charge neutralization. The width of the return current region is of the order of a gyroradius of an ion accelerated up to the spacecraft potential. If this width is greater than the spacecraft width, then some of the return electrons can propagate past the spacecraft. This flow is charge neutralized by plasma ions behind the spacecraft being accelerated outwards and plasma electrons in the same region being drawn into the spacecraft.

The electromagnetic simulations have confirmed that whistler waves can be produced in connection with electron beam injection in the ionosphere. They have shown that the beam-plasma interaction leads to the formation of current structures which act like an antenna and emit whistler waves in a coherent manner via a Cerenkov resonance. This coherent process allows the production of the whistler waves even though the beam width is less than one wavelength. The generation efficiency is comparable to the Spacelab 2 observations. The whistler waves propagate at angles substantially away from the resonance cone and are predominantly electromagnetic in nature.

PART B. SPACECRAFT POTENTIAL CONTROL VIA INDIUM ION BEAM INJECTION

XII. INTRODUCTION

A recurring difficulty for space satellites making plasma observations concerns the accurate measurement of very cold plasma and/or low frequency electric fields during periods of high electrostatic surface potentials. Although scientific spacecraft have been equipped with conductive surfaces to eliminate differential charging between sunlit and shadowed surfaces, the fundamental problem of overall electrostatic charging remains. *Olsen* [1982] used the reduction of the spacecraft potential during a transit from sunlight into eclipse for the identification of a cold plasma population previously undetected due to the masking effect of the positive surface potential.

The electrostatic potential of the spacecraft is a consequence of the current equilibrium between charged particles impacting on the surface and charges leaving the surface, such as photo-electrons, sputter-induced charged secondary particles, and artificially ejected charges [*Pedersen et al.*, 1987]. The extreme values of the electrostatic potential may range from less than −1000 Volts up to +1000 Volts [*Garrett*, 1981]. To maintain the spacecraft potential near the ambient plasma potential, an ion emission system that is small in size and resources is needed. A major constraint on such a system comes from the fact that its spacecraft resource requirements remain within a reasonable ratio with other instruments on the spacecraft and it should also be "quiet" in the sense of not interfering with other instruments onboard. Keeping these requirements in mind it was decided to develop new systems based on the use of liquid indium [*Schmidt et al.*, 1989].

Included in the instrumentation package for the upcoming Cluster and Geotail satellites will be a small compact ion emitter that contains a tiny amount of indium carried in a heater controlled containment device. Once the indium is heated to well above its melting point, the liquid metal flows due to surface tension along the shaft of a small needle. At its top the indium is ionized by field emission and emitted. The typical beam drift kinetic energy is 5 to 6 keV.

The main concern of the research we have carried out has been to examine whether the emitted indium ion beam can be unstable to electrostatic plasma instabilities for the various emitted beam and background conditions. For this study we restrict ourselves to a standard size spacecraft with conductive surfaces and to orbits outside the plasmasphere. Eclipse conditions are ignored and therefore the sunlit spacecraft will charge positive due to the dominance of sun-induced photo-electrons. The goal of the linear theory study is to identify any unstable wave modes that can occur such that effects that may result from these instabilities can be distinguished from other plasma physical processes. The detailed parameter search quantifies under what conditions the indium ion beam can be emitted in such a way that an instability can be turned on or off during the mission.

XIII. OPERATING PRINCIPLES OF THE LIQUID METAL ION SOURCE (LMIS)

The ion emitter [*Rüdenauer et al.*, 1988] is a "solid-needle" type liquid metal ion source using indium as charged material [*Dixon and von Engle*, 1980]. Indium has an atomic number of 49 and its mass is 114.82. A tungsten needle with a tip radius of typically 2 to 15 μ is mounted in the indium reservoir which is attached to a heater. If the needle is well wetted by the metal, then the electrostatic stress at the needle's tip pulls the liquid indium towards the extractor electrode. This stress is counteracted by the surface tension. The resulting equilibrium is characterized by a stable field emission from a liquified cone (Taylor cone) with a tip radius of 1 to 5 nm. The evaporation and resulting ionization leads to the emission of positively charged ions from the Taylor cone. Typical current densities at the cone apex are of the order of $10^6 \text{cm}^{-2}\text{sr}^{-1}\text{A}$ for a beam energy of 10 keV. Ions leaving the surface are constantly replenished by hydrodynamic flow of liquid indium from the reservoir to the tip of the needle.

The typical operating characteristics of the LMIS require an extraction high voltage of 5 kV applied between extraction electrode and needle/reservoir. An emission current of 10 μA requires a supply current of about 20 μA, mostly due to focussing losses. The heater power required to maintain the indium reservoir well above the melting temperature is about 0.4 W. The beam divergence at the orifice is better than 15 (half-width), and the beam temperature $\Delta E/E$ is better than 10^{-3} at 1 μA, with a weak dependence on the applied extraction voltage. The beam temperature depends on the emission current, which can be set by adjusting a current limiter inside the high voltage power supply. For small emission currents, around 1 μA, the measured beam temperature is of the order of 40 eV. Increasing the emission current up to 10 μA results in an increasing beam temperature (600 eV) that is mostly due to the appearance of a high energy tail.

For the linear theory study, we take the In$^+$ beam drift energy to be 5 keV, which corresponds to a drift speed of about 91.3 km/s. The temperature of the beam, as explained, is variable depending on the emission current setting and can range from 40 to 600 eV; the beam

thermal speed will be a parameter that will be varied during the linear theory study.

XIV. LINEAR THEORY

A linear theory parameter search has been carried out to investigate whether particular combinations of ambient plasma parameters and emission modes of the indium ion beam exist such that electrostatic plasma instabilities may be excited. We consider a three species plasma with (1) an indium ion beam, (2) background electrons, and (3) background ions. The background plasma parameters vary depending on where the satellite is at the time of beam emission. For our study we considered four different background regions: the solar wind, the lobe, the plasma sheet boundary layer, and the central plasma sheet. Typical plasma parameters for each of these regions used in this study are found in Table 3, and are based on previous observations made in each region [*Frank*, 1985; *Lui*, 1987; *Rosenberg and Whipple*, 1990].

TABLE 3. Listed here are typical observed parameters for each of the four regions under consideration

Region	T_i/T_e	ω_{pe}/Ω_e	$T_e(eV)$	$n_e(cm^{-3})$
CPS	5	5–20	>1000	1
PSBL	2	5	~500	0.1
Lobe	2	1	<100	0.01
Solar Wind	<2	55–200	10	1-10

To understand the basic physics of unstable wave modes possible for this type of configuration, we first consider a cold plasma with magnetized electrons and unmagnetized ions. Following *Mikhailovskii* [1975], the dispersion relation can be written as

$$0 = 1 - \frac{\omega_{pe}^2 \sin^2\theta}{\omega^2 - \Omega_e^2} - \frac{\omega_{pe}^2 \cos^2\theta}{\omega^2} - \frac{\omega_{pi}^2}{\omega^2} - \frac{\omega_{pb}^2}{(\omega - kU)^2} \tag{1}$$

where ω_{pe}, ω_{pi}, and ω_{pb} are the plasma frequencies of the background electrons, background ions and beam ions, respectively, Ω_e is the electron gyrofrequency, θ is the angle between the wavenumber $\vec{k}$ and the external

magnetic field, and $\vec{U}$ is the indium beam drift velocity. We assume that $\vec{k}$ and $\vec{U}$ are aligned. The frequency ω is complex with $\omega = \omega_r + i\gamma$.

An unstable interaction between the beam mode and the lower hybrid mode occurs at very oblique wave propagation ($\theta \sim 90°$) when $\omega_r = \omega_{lh} \approx kU$, where the lower hybrid frequency is given by

$$\omega_{lh} = \frac{\omega_{pi}}{\sqrt{1 + \omega_{pe}^2/\Omega_e^2}} \tag{2}$$

in the limit of unmagnetized ions, i.e., $\omega_{pi} \gg \Omega_i$. The growth rate for this instability is given by

$$\gamma \approx \frac{\omega_{lh}\alpha^{1/3}}{[\, 1 + (m_i/m_e)\cos^2\theta]^{1/3}} \tag{3}$$

where $\alpha = n_b m_i / n_i m_b \ll 1$, n_b and m_b are the beam density and mass, n_i and m_i are the background ion density and mass, and m_e is the background electron mass. The wave growth is due to a fluid-type isntability driven by the net drift between the beam and background plasma, and it is interesting to note from equation (3) that the growth rate maximizes when $\theta = 90°$.

If we consider the case where the indium beam is not strictly cold, but is approximated by a Maxwellian velocity distribution, a beam driven lower hybrid instability with real frequency given by equation (2) is still present, but the growth rate is modified and can be expressed as

$$\gamma \approx \left(\frac{U}{v_{tb}}\right)^2 \frac{\alpha\omega_{lh}}{1 + (m_i/m_e)\cos^2\theta} \tag{4}$$

where v_{tb} is the beam thermal speed. As in the cold plasma case, the instability maximizes for transverse wave propagation ($\theta = 90°$), but for a warm beam the growth rate is sensitive to the beam drift to thermal speed ratio U/v_{tb}, such that as the beam temperature increases for a given drift speed, the growth rate will decrease.

To study the parametric dependence of this instability for the different background regions and beam emission modes, we have solved the fully magnetized warm electrostatic dispersion relation numerically. The form for the general electrostatic dispersion relation can be found in *Harris* [1959] or *Stix* [1962]. An example of the dispersion relation for the indium ion beam ejected while the satellite is in the plasma sheet boundary layer is

shown in Figure 16. The beam drift speed to thermal speed ratio used for this figure is $U/v_{tb} = 17$ and the beam density is $n_b/n_e = 0.5$. Plotted is frequency versus wavenumber with the real frequency shown by the solid line and the growth rate shown by the dashed line. In Figure 16, the wave propagation angle is varied and the results confirm that found from equations (3) and (4), whereby the growth rate maximizes for purely transverse wave propagation ($\theta = 90°$). Keep in mind that the beam is directed parallel to $\vec{k}$, which means that maximum wave growth occurs for the beam being emitted 90° to the external magnetic field. The real frequency at maximum wave growth is less than the lower hybrid frequency given in equation (2), due to warm plasma effects of the background ions.

Now maintaining transverse wave propagation ($\theta = 90°$) to find maximum wave growth, we plot in Figures 17, 18, 19, and 20 the dispersion relation for beam emission in the central plasma sheet, plasma sheet boundary layer, solar wind, and lobe, respectively (the background parameters are listed in Table 3). The format for these figures is the same as in Figure 16, and the beam density is the same; however, the ratio U/v_{tb} is varied (keeping U fixed corresponding to a beam drift energy of 5 keV) for each region to find the instability threshold. As expected from equation (4) the growth rate decreases as U/v_{tb} decreases, which corresponds to an increase in the beam temperature. From Figures 17 through 20 it can be seen that the central plasma sheet has the lowest threshold for the beam instability as a function of beam temperature, which means that the indium beam can be fairly warm and still drive an instability there. The lobe, on the other hand, has the highest threshold whereby the beam must be relatively cool (low emission current) for an instability to exist.

Plasma Sheet Boundary Layer
Dispersion Relation
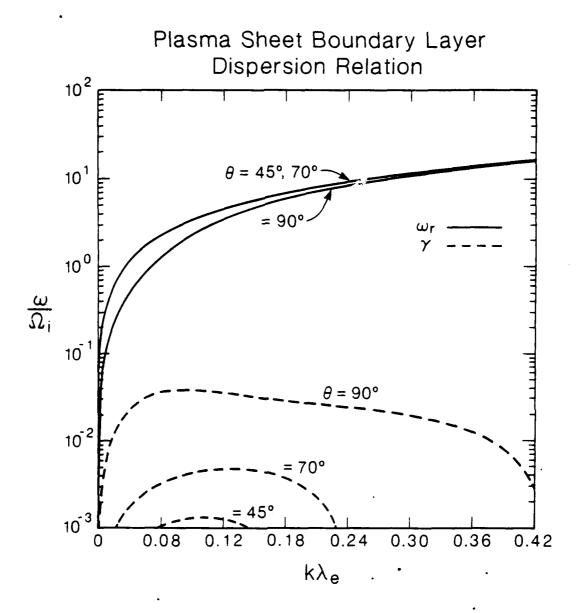
Figure 16. This figure shows the dispersion of low frequency waves found from numerical solutions of the general warm plasma dispersion relation for an indium ion beam emitted while the satellite is in the plasma sheet boundary layer. Plotted is frequency (normalized to the background ion gyrofrequency) versus wavenumber (times the electron Debye length). The solid line corresponds to the real frequency and the growth rates are shown by the dashed line for three different wave propagation angles. Note the growth rate maximizes for transverse wave propagation.

Central Plasma Sheet
Dispersion Relation
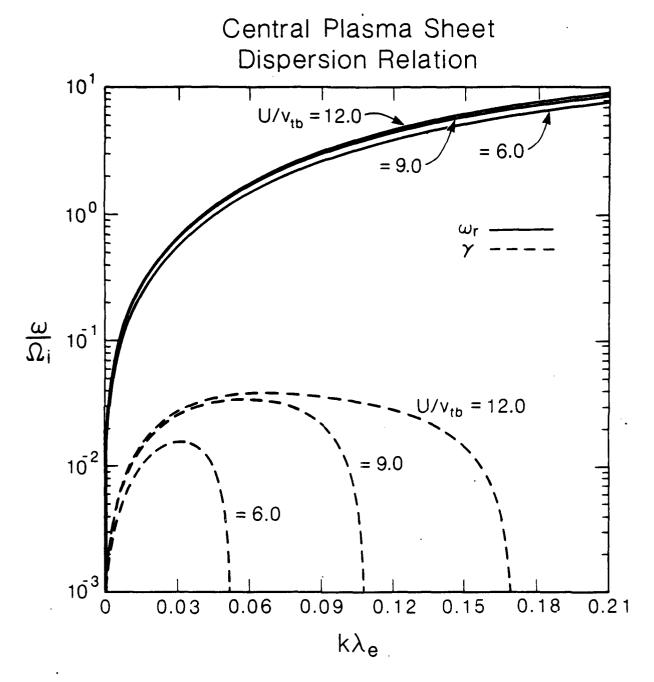
Figure 17. The wave dispersion relation when the indium beam is emitted in the central plasma sheet. The format is the same as Figure 16, but here the ratio U/v_{tb} is varied and the lowest value where there is still an appreciable instability is shown. The background plasma parameters are found in Table 3. In this case, if U/v_{tb} falls below 6, no instability is possible.
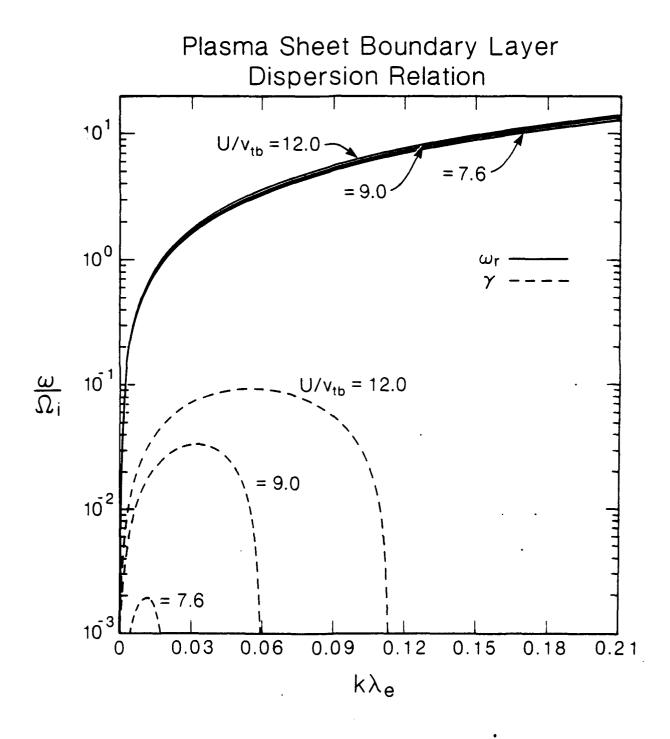
Figure 18. <u>Dispersion relation for beam emission in the plasma sheet boundary layer. The format is the same as in Figure 17, with the background parameters found from Table 3.</u>

Solar Wind
Dispersion Relation

Figure 19. <u>Dispersion relation for beam emission in the solar wind. The format is the same as in Figure 17, with the background parameters found from Table 3.</u>

Lobe Dispersion Relation

$U/v_{tb} = 14.1, 14.5, 15.3$

ω_r ———

γ − − − −

$U/v_{tb} = 15.3$

$= 14.5$

$= 14.1$

$\dfrac{\omega}{\Omega_i}$

$k\lambda_e$

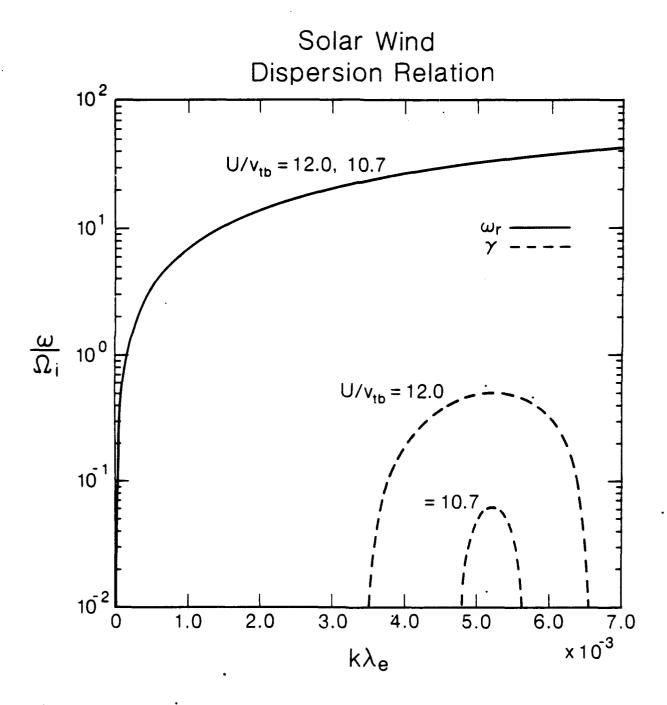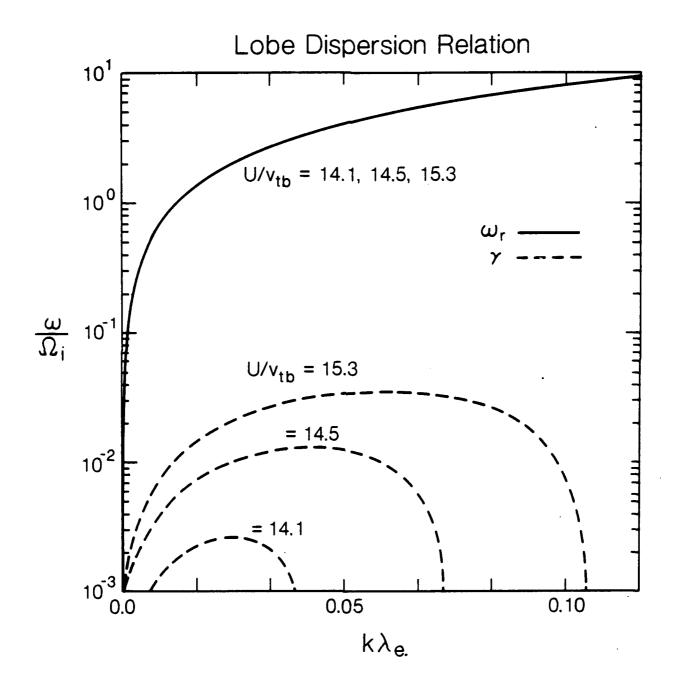Figure 20. <u>Dispersion relation for beam emission in the lobe. The format is the same as in Figure 17, with the background parameters found from Table 3. Note that this region has the highest threshold for instability compared to the others.</u>

XV. SUMMARY

An indium ion beam device will be placed on future satellites such as Geotail and Cluster to control the spacecraft potential. A study has been carried out to see if the emitted indium ion beam can be unstable when the satellite is in various regions of the Earth's magnetosphere and solar wind. Linear theory for electrostatic waves shows that an ion beam driven lower hybrid instability can be excited with maximum growth at wave propagation (and beam emission) transverse to the external magnetic field.

Numerical results from the linear theory parameter search show that for the expected indium beam conditions and typical parameters for the background plasma that the central plasma sheet will have the lowest threshold for instability, while the lobe will have the highest. Since the emission current, which controls the beam thermal speed, can be varied during the satellite mission, the linear theory results can be tested directly by changing the current and using observed wave data to see whether an instability in the right frequency range is excited and turns on or off according to the stability criteria. Also, depending on the orientation of the beam emitter with the external magnetic field, the linear theory conclusion that maximum wave growth will occur for transverse emission can be tested.

REFERENCES

Beghin, C., J.P. Lebreton, B.N. Maehlum, J. Troim, P. Ingsoy, and J.L. Michau, Phenomena induced by charged particle beams, *Science, 225,* 188 (1984).

Bernstein, W., H. Leinbach, P.J. Kellogg, S.J. Monson, and T.J. Hallinan, Further laboratory measurements of the beam plasma discharge, *J. Geophys. Res., 84,* 271 (1979).

Cartwright, D.C., and P.J. Kellogg, Observations of radiation from an electron beam artificially injected into the ionosphere, *J. Geophys. Res., 79,* 439 (1974).

Dawson, J.M., and R. Shanny, Some investigations of nonlinear behavior in one-dimensional plasmas, *Phys. Fluids, 11,* 1506 (1968).

Dechambre, M., Yu.V. Kushnerevsky, J. Lavergnat, R. Pellat, S.A. Pulinets, and V.V. Seleger, Waves observed by the ARAKS experiment: The whistler mode, *Ann. Geophys., 36,* 351 (1980).

Dixon, A.J., and A. vonEngle, Studies of field emission gallium ion sources, *Inst. Conf. Ser., 54,* 292 (1980).

Farrell, W.M., D.A. Gurnett, P.M. Banks, R.I. Bush, and W.J. Raitt, An analysis of whistler mode radiation from the Spacelab 2 electron beam, *J. Geophys. Res., 93,* 153 (1988).

Frank, L.A., Plasmas in the earth's magnetotail, *Space Sci. Rev., 42,* 211 (1985).

Garrett, H.B., The charging of spacecraft surfaces, *Rev. Geophys. Space Sci., 19,* 744 (1981).

Grandal, B. (Ed.), *Artificial Particle Beams in Space Plasma Studies,* 704 pp., Plenum Publishing Co., New York, New York (1982).

Gurnett, D.A., W.S. Kurth, J.T. Steinberg, P.M. Banks, R.I. Bush, and W.J. Raitt, Whistler-mode radiation from the Spacelab 2 electron beam, *Geophys. Res. Lett., 13,* 225 (1986).

Harris, E.G., Unstable plasma oscillations in a magnetic field, *Phys. Rev. Lett., 2,* 34 (1959).

Hockney, R.W., Formation and stability of virtual electrodes in a cylinder, *J. Appl. Phys., 38,* 4166 (1968).

Inan, U.S., M. Pon, P.M. Banks, P.R. Williamson, W.J. Raitt, and S.D. Shawhan, Modulated beam injection from Space Shuttle during

magnetic conjunctions of STS 3 and DE 1 satellite, *Radio Sci., 19*, 487 (1984).

Kellogg, P.J., and S.J. Monson, Rocket borne accelerator results pertaining to the beam plasma discharge, *Adv. Space Res., 1*, 61 (1981).

Kellogg, P.J., H.R. Anderson, W. Bernstein, R.J. Hallinan, R.W. Holzworth, R.J. Jost, H. Leinbach, and E.P. Szuszewicz, Laboratory simulation of injection of particle beams in the ionosphere, in *Artificial Particle Beams in Space Plasma Studies*, NATO Adv. Study Inst. Ser., Ser. B, Vol. 79, edited by B. Grandal, p. 289, Plenum Publishing Co., New York, New York (1982).

Kellogg, P.J., S.J. Monson, W. Bernstein, and B.A. Whalen, Observations of waves generated by electron beams in the ionosphere, *J. Geophys. Res., 91*, 12,065 (1986).

Lui, A.T.Y., Road map to magnetotail dynamics, *Magnetotail Physics*, edited by A.T.Y. Lui, p. 1, Johns Hopkins University Press, Baltimore, MD (1987).

Maehlum, B.N., Beam-plasma experiments, *Comput. Phys. Commun., 49*, 119 (1988).

Mansfield, V.N., Radiation from a charged particle spiraling in a cold magnetoplasma, *Astrophys. J., 147*, 672 (1967).

Mikhailovskii, A.B., *Theory of Plasma Instabilities*, McGraw-Hill, New York, NY (1975).

Monson, S.J., and P.J. Kellogg, Ground observations of waves at 2.96 MHz generated by an 8 to 40 keV electron beam in the ionosphere, *J. Geophys. Res., 83*, 121 (1978).

Myers, N.B., W.J. Raitt, A.B. White, P.R. Williamson, R.I. Bush, P.M. Banks, and S. Sasaki, The initial transient charging of a vehicle in space during electron emission measured by the CHARGE-2 rocket payload, *EOS, 65*, 1170 (1986).

Okuda, H., and M. Ashour-Abdalla, Propagation of a nonrelativistic electron beam in three dimensions, *J. Geophys. Res., 95*, 2389 (1990a).

Okuda, H., and M. Ashour-Abdalla, Injection of an overdense electron beam in space, *J. Geophys. Res., 95*, 21,307 (1990b).

Olsen, R.C., The hidden ion population of the magnetosphere, *J. Geophys. Res., 87*, 3481 (1982).

Pedersen, A., C.A. Cattell, C.G. Fälthammar, V. Formisano, P.A. Lindqvist, F. Mozer, and R. Torbert, Quasi-static electric field measurements with spherical double probes on the GEOS and ISEE satellites, *Space Sci. Rev., 37,* 269 (1987).

Pritchett, P.L., Electromagnetic particle simulation codes, in *Space plasma simulations,* edited by M. Ashour-Abdalla and D.A. Dutton, p. 17, D. Reidel, Hingham, Mass (1985).

Pritchett, P.L., Spatial coherence and electromagnetic wave generation during electron beam experiments in space, in *Advances in Space Research 1990,* in press (1991).

Pritchett, P.L., and R.M. Winglee, The plasma environment during particle beam injection into space plasmas: 1. Electron beams, *J. Geophys. Res., 92,* 7673 (1987).

Raitt, W.J., P.R. Williamson, P.M. Banks, N.B. Myers, and N. Kawashima, High time resolution measurements of rocket potential changes induced by electron beam emissions, in *Proceedings of the 14th International Symposium on Space Technology and Sciences,* p. 1501 (1984).

Rosenberg, M., and E. Whipple, Propagation and beam-plasma interactions of the EDI beam, *Proceedings of the AIAA 21st Fluid Dynamics, Plasma Dynamics and Lasers Conference, AAIA 90-1567,* 1 (1990).

Rüdenauer, F.G., W. Steiger, H. Arends, M. Fehringer, and R. Schmidt, A liquid metal ion source for space application, *J. de Physique, 49,* 161 (1988).

Sasaki, S., K.-I. Oyama, N. Kawashima, W.J. Raitt, and N.B. Myers, VLF and HF wave characteristics observed from an active experiment tethered mother/daughter rocket payload (CHARGE-2), *EOS, 67,* 1170 (1986).

Schmidt, R., H. Arends, K. Torkar, and N. Valavanoglou, Novel methods for active spacecraft potential control, *AGU Geophysical Monograph* (1989).

Shawhan, S.D., G.B. Murphy, P.M. Banks, P.R. Williamson, and W.J. Raitt, Wave emissions from DC and modulated electron beams on STS3, *Radio Sci., 19,* 471 (1984).

Smith, R.L., R.A. Helliwell, and I.W. Yabroff, A theory of trapping of whistlers in field-aligned columns of enhanced ionization, *J. Geophys. Res., 65*, 815 (1960).

Stix, T.H., *Theory of Plasma Waves*, McGraw-Hill, New York, NY (1962).

Winckler, J.R., The application of artificial electron beams to magnetospheric research, *Rev. Geophys., 18*, 659 (1980)

Winglee, R.M., and P.J. Kellogg, Electron beam injection during active experiments, 1, Electromagnetic wave emissions, *J. Geophys. Res., 95*, 6167 (1990).

Winglee, R.M., and P.L. Pritchett, Space-charge effects during the injection of dense electron beams into space plasmas, *J. Geophys. Res., 92*, 6114 (1987).

Winglee, R.M., and P.L. Pritchett, Comparative study of cross-field and field-aligned electron beams in active experiments, *J. Geophys. Res., 93*, 5823 (1988).

MISSION

OF

ROME LABORATORY

Rome Laboratory plans and executes an interdisciplinary program in research, development, test, and technology transition in support of Air Force Command, Control, Communications and Intelligence (C^3I) activities for all Air Force platforms. It also executes selected acquisition programs in several areas of expertise. Technical and engineering support within areas of competence is provided to ESD Program Offices (POs) and other ESD elements to perform effective acquisition of C^3I systems. In addition, Rome Laboratory's technology supports other AFSC Product Divisions, the Air Force user community, and other DOD and non-DOD agencies. Rome Laboratory maintains technical competence and research programs in areas including, but not limited to, communications, command and control, battle management, intelligence information processing, computational sciences and software producibility, wide area surveillance/sensors, signal processing, solid state sciences, photonics, electromagnetic technology, superconductivity, and electronic reliability/maintainability and testability.